

Electrochemical CO₂ Reduction at Silver from a Local Perspective

Xinwei Zhu, Jun Huang, and Michael Eikerling*

Cite This: *ACS Catal.* 2021, 11, 14521–14532

Read Online

ACCESS |



Metrics & More



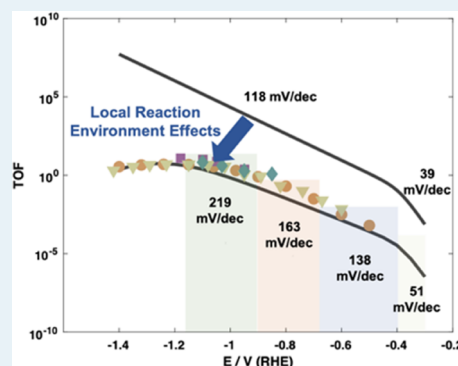
Article Recommendations



Supporting Information

ABSTRACT: The electrochemical reduction of CO₂ to chemical fuels and value-added chemicals is a viable pathway to store renewably generated electrical energy and to mitigate the negative impact of anthropogenic CO₂ production. Herein, we study how the local reaction environment dictates the mechanism and kinetics of CO₂ reduction to CO at an Ag electrode. The local reaction environment is determined using a hierarchical model that accounts for multistep reaction kinetics, specific surface charging state at a given electrode potential, and mass transport phenomena. The model reveals vital mechanistic insights into the reaction behavior. The increasing Tafel slope with overpotential is seen to be influenced by the surface charging relation and mass transport effects. In addition, the decrease of the CO current density at high overpotentials is found to be caused not only by the decrease in CO₂ concentration due to mass transport, surface charge effects, and pH increase but also by lateral interactions between HCOO_{ad}, COOH_{ad}, and H_{ad}. Moreover, we explore how the electrolyte properties, including bicarbonate concentration, solvated cation size, and CO₂ partial pressure, tune the local reaction environment.

KEYWORDS: CO₂ electrochemical reduction, silver electrode, local reaction environment, surface charge effects, mass transport, lateral interactions



INTRODUCTION

Electricity production from renewable energy sources will have to grow at an escalating pace if the direst consequences of climate change are to be averted. On the path toward a defossilized, environmentally benign, and sustainable energy economy, two pressing challenges must be addressed: (i) the balance of anthropogenic CO₂ production must be rapidly reduced to net zero (and then net negative) and (ii) the development of infrastructure concepts and technologies for large-scale and long-term energy storage must keep pace with the growth of renewable power sector.

The conversion of CO₂ into chemical fuels (and value-added chemicals), driven with a supply of renewable energy, is the most compelling option to tackle both of these challenges at once.^{1–4} However, CO₂ electrolysis is limited by a low energy efficiency and the usually low current density of fuel production. The critical CO₂ electro-reduction reaction (CO₂RR) exhibits notoriously sluggish kinetics as well as a low selectivity toward the formation of convenient transportation fuels and benign media for energy storage, such as ethanol, propanol, or butanol. The latter products exhibit high energy density (J/L) and specific energy (J/kg) and are liquid at ambient conditions and therefore easy to store.

CO is a key intermediate of the CO₂RR to C₂₊ alcohols.^{3,5} Au and Ag are known as the most active and selective catalysts for CO₂RR to CO.^{2,5–7} Albeit being a seemingly simple process, CO₂ reduction to CO at Ag has not been completely understood and remains a source of controversial debates.⁷

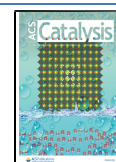
Tafel analysis is a vital mechanistic probe of multistep reactions. Different Tafel slopes (denoted as *b*) that have been reported for CO₂RR at Ag can be associated with distinct reaction mechanisms and pathways or rate-determining steps (RDSs). Rosen et al. determined *b* = 134 and 64 mV/dec on polycrystalline and nanostructured Ag, respectively, in the range of low overpotentials. Based on these data, they concluded that the first proton-coupled electron transfer (PCET) step is the RDS at polycrystalline Ag, while the second proton transfer (PT) step was identified as the RDS at nanostructured Ag.⁸ Dunwell et al. obtained 59 mV/dec on both polycrystalline Ag and nanostructured Ag at lower overpotentials, leading them to claim that the RDS at both electrodes is a PT step following upon an initial electron transfer step or PCET step.⁹ Moreover, they found a Tafel slope of 118 mV/dec at higher overpotentials in their experiments, which was ascribed to mass transport effects and/or site blocking due to cation accumulation in the outer Helmholtz plane (OHP).

First-principles computational studies have also reported different RDSs, including the hydrogenation of adsorbed CO₂

Received: October 18, 2021

Revised: November 2, 2021

Published: November 17, 2021



to COOH_{ad} ¹⁰ or the PCET step of COOH_{ad} to CO_{ad} .¹¹ The incongruent findings and interpretations may arise from the neglect or insufficient consideration of the local reaction environment (LRE) that prevails at the surface of the electrocatalyst, which exerts a marked impact on the apparent kinetics.^{12–16} By the LRE, we refer to not only the interfacial liquid region of several nanometers thickness, in which the electric potential and ion concentrations exhibit strong spatial variations, but also the surface of the solid catalyst, which is covered with multiple types of adsorbed intermediates.

Surface-enhanced infrared spectroscopy has been used to detect the concentration gradients in the region of 5–10 nm away from the electrode.¹² However, direct experimental probes of the LRE at the OHP are currently out of reach. Theoretical modeling has to step up to fill this gap in understanding, which has major implications for our ability to find or design new electrocatalyst materials and scrutinize their utility under realistic reaction conditions. A comprehensive treatment of the LRE should consider ion transport in the electrolyte solution that is dictated by the excess charge density on the electrode surface, as well as the formation and desorption of multiple adsorbed intermediates that interact with each other and with solution species in a complex way. To date, a comprehensive theoretical treatment that accounts for these phenomena has not been devised for the CO_2RR at Ag. Several models have been developed to focus on the species transport in solution.^{10,17–20} However, these approaches do not account for the surface charging relation of the electrode material. Ringe et al. developed a multiscale model for the CO_2RR at a gold electrode that included surface charging effects.²¹ Competitive reactions and lateral interactions were found to be minor effects in their case and therefore were not considered. However, DFT calculations have revealed the importance of interactions between intermediates HCOO_{ad} , COOH_{ad} , and H_{ad} on Ag,²² stressing the importance of considering lateral interactions between adsorbates in kinetic modeling.

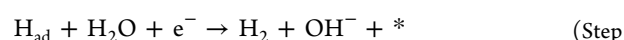
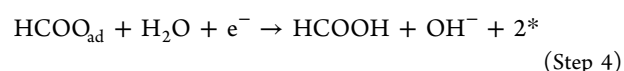
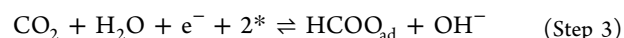
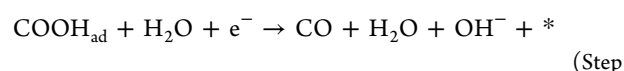
In this study, we develop a comprehensive model with the aim to describe the LRE for CO_2RR at a planar Ag electrode. Our hierarchical model links a microkinetic model that considers CO pathway, H_2 pathway, and HCOOH pathway with a mass transport model that seamlessly integrates the electric double layer (EDL) level with a characteristic scale of several nanometers thickness and the electroneutral diffusion layer of several tens of micrometers thickness. Armed with this approach, we unravel why the CO partial current density first increases and then decreases with overpotential, and how the Tafel slope is determined by the intrinsic kinetics and the LRE. Then, we tune the LRE by varying the electrolyte properties, including the concentration of bicarbonate, the type of electrolyte cation, and the partial pressure of CO_2 .

MODEL DEVELOPMENT

We model the reduction of CO_2 on a planar Ag(110) electrode in 0.1 M KHCO_3 solution under ambient conditions (25 °C, 101.3 kPa). The potential of interest is between –0.3 and –1.4 V. Hereinafter, all potentials are referenced to the reversible hydrogen electrode, RHE, unless otherwise noted. In this potential range, several reactions may occur in parallel, including the main reaction, that is, CO_2 reduction to CO, and the competitive reactions, i.e., CO_2 reduction to HCOOH and the hydrogen evolution reaction (HER).^{23,24} The model consists of a microkinetic submodel that determines the

adsorbate coverages and current densities and a mass transport submodel that determines the distributions of the solution phase potential and species concentrations in the electrolyte solution.

Microkinetic Model. The reaction mechanism used in this model includes three pathways, the CO pathway (Steps 1 and 2), the HCOOH pathway (Steps 3 and 4), and the H_2 pathway (Steps 5 and 6), forming three main products of CO_2 RR on Ag.^{23,24}



We make the following simplifications: (1) The reverse reactions of Steps 2, 4, and 6 are neglected considering that the solubilities of CO and H_2 are quite low,²⁵ and the concentration of HCOOH is negligible due to the low formation rate.^{24,26} (2) The desorption of CO_{ad} is very fast,^{8,27} so we combine COOH_{ad} reduction to CO_{ad} and CO_{ad} desorption into Step 2. (3) The Tafel step of the HER is not considered since it is not energetically favorable at Ag.¹⁰ (4) The possible interconversion of COOH_{ad} and HCOO_{ad} is not considered. $\theta_{\text{COOH}_{\text{ad}}} \approx 0$ because COOH_{ad} hardly adsorbs on Ag as demonstrated with DFT studies.²² The simulated coverage of COOH_{ad} is less than 1.8×10^{-4} in this work. Therefore, the conversion of COOH_{ad} to HCOO_{ad} can be neglected. In addition, DFT studies have found that $\Delta G_{\text{COOH}_{\text{ad}}} - \Delta G_{\text{HCOO}_{\text{ad}}} \approx 1$ eV on Ag,²² which means that the conversion of HCOO_{ad} to COOH_{ad} is energetically unfavorable. (5) We consider all reaction steps as PCET steps, as in refs 28–30. We notice that sequential proton and electron transfer were also proposed.³¹ In addition, the adsorption of CO_2 was shown to be the RDS on gold.²¹ To date, there is still no consensus on the reaction mechanisms and this thus remains an important topic for future research. (6) The proton precursor here is H_2O not H^+ because the proton concentration is 1.58×10^{-7} M in 0.1 M KHCO_3 solution (pH = 6.8), which can only support a current density in the order of 10^{-3} mA/cm², as shown in Figure S1 in the Supporting Information (SI).

Based on the reaction equations, we solve the following system of rate equations at steady state

$$\frac{d\theta_{\text{COOH}_{\text{ad}}}}{dt} = \nu_1 - \nu_2 = 0 \quad (1)$$

$$\frac{d\theta_{\text{HCOO}_{\text{ad}}}}{dt} = \nu_3 - \nu_4 = 0 \quad (2)$$

$$\frac{d\theta_{\text{H}_{\text{ad}}}}{dt} = \nu_5 - \nu_6 = 0 \quad (3)$$

where $\theta_{\text{COOH}_{\text{ad}}}$, $\theta_{\text{HCOO}_{\text{ad}}}$, and $\theta_{\text{H}_{\text{ad}}}$ are coverages and ν_i is the reaction rate of step i . For the latter, we have the following relations

$$v_1 = k_1 c_{\text{CO}_2}^{\text{OHP}} \theta_0 - k_{-1} \theta_{\text{COOH}_{\text{ad}}} c_{\text{OH}^-}^{\text{OHP}} \quad (4)$$

$$v_2 = k_2 \theta_{\text{COOH}_{\text{ad}}} \quad (5)$$

$$v_3 = k_3 c_{\text{CO}_2}^{\text{OHP}} \theta_0^2 - k_{-3} \theta_{\text{HCOO}_{\text{ad}}} c_{\text{OH}^-}^{\text{OHP}} \quad (6)$$

$$v_4 = k_4 \theta_{\text{HCOO}_{\text{ad}}} \quad (7)$$

$$v_5 = k_5 \theta_0 - k_{-5} \theta_{\text{H}_{\text{ad}}} c_{\text{OH}^-}^{\text{OHP}} \quad (8)$$

$$v_6 = k_6 \theta_{\text{H}_{\text{ad}}} \quad (9)$$

with $\theta_0 = 1 - \theta_{\text{COOH}_{\text{ad}}} - 2\theta_{\text{HCOO}_{\text{ad}}} - \theta_{\text{H}_{\text{ad}}}$ being the vacancy coverage (free sites), and $c_{\text{CO}_2}^{\text{OHP}}$ and $c_{\text{OH}^-}^{\text{OHP}}$ being, respectively, the concentrations of CO_2 and OH^- at the OHP that need to be determined from the mass transport model. Rate constants of the forward and reverse reactions, k_i and k_{-i} , respectively, are calculated from transition-state theory

$$k_{\pm i} = \frac{k_B T}{h} \exp\left(-\frac{\Delta G_{a,\pm i}}{k_B T}\right) \quad (10)$$

where k_B is the Boltzmann constant, h is Planck's constant, and T is the temperature. Activation energies, $G_{a,\pm i}$ for the forward and backward reaction under standard conditions (298 K, 1 bar pressure, pH = 0) are obtained using the Bronsted–Evans–Polanyi (BEP) relation

$$G_{a,i} = G_{a,i}^{\text{eq}} + \beta_i \Delta G_i \quad (11)$$

$$G_{a,-i} = G_{a,-i}^{\text{eq}} - (1 - \beta_i) \Delta G_i \quad (12)$$

where $G_{a,i}^{\text{eq}}$ and $G_{a,-i}^{\text{eq}}$ are activation energies of step i for the forward and backward reactions under standard equilibrium conditions, respectively, β_i is the transfer coefficient, and ΔG_i is the reaction free energy. Note that $G_{a,i}^{\text{eq}} = G_{a,-i}^{\text{eq}}$ because $\Delta G_i = 0$ at the equilibrium state.

When the applied potential deviates from the equilibrium potential E_i^{eq} , the reaction Gibbs energies will shift according to

$$\Delta G_i = e(\varphi_M - \varphi_{\text{OHP}} - E_i^{\text{eq}}) \pm \sum_{X_j} \xi_{X_j, X_i} \theta_{X_j} \quad (13)$$

where e is the elementary charge, φ_M is the applied potential relative to the standard hydrogen electrode (SHE), φ_{OHP} is the potential at the OHP, and $\xi_{X_j, X_i} \theta_{X_j}$ represents the variation in the Gibbs free energy caused by lateral interactions between intermediates involved in step i , X_i , and other intermediates X_j (COOH_{ad} , HCOO_{ad} , and H_{ad}), with ξ_{X_j, X_i} being the lateral interaction parameter.³² $\xi_{\text{COOH}_{\text{ad}}, X_i} \theta_{\text{COOH}_{\text{ad}}}$ can be neglected because $\theta_{\text{COOH}_{\text{ad}}} \approx 0$. The detailed expressions for ΔG_i can be found in the SI.

The equilibrium potential of step i at the standard state, E_i^{eq} , is calculated using the Nernst equation

$$E_i^{\text{eq}} = -\frac{\Delta G_i^0}{e} \quad (14)$$

with ΔG_i^0 being the reaction free energy of step i at the standard state, which can be calculated using DFT.³³ The results are shown in Table 1.

$\theta_{\text{COOH}_{\text{ad}}}$, $\theta_{\text{HCOO}_{\text{ad}}}$, and $\theta_{\text{H}_{\text{ad}}}$ can be obtained by solving eqs 1–3. The partial current densities are given by

Table 1. Reaction Parameters Used in This Model, Including Standard Equilibrium Potential, E_i^{eq} , Activation Energy, $G_{a,i}^{\text{eq}}$, and Transfer Coefficient, β_i , of Step i

step i	ΔG_i^0	$E_i^{\text{eq}}/\text{V (SHE)}$	$G_{a,i}^{\text{eq}}/\text{eV}$	β_i
1	$\Delta G_{\text{COOH}_{\text{ad}}}^0 - \Delta G_{\text{CO}_2}^0$	−1.2 ²³	0.53 ¹⁰	0.5
2	$\Delta G_{\text{CO}_{\text{ad}}+\text{H}_2\text{O}}^0 - \Delta G_{\text{COOH}_{\text{ad}}}^0$	0.5 ²³	1.4 ¹¹	0.5
3	$\Delta G_{\text{HCOO}_{\text{ad}}}^0 - \Delta G_{\text{CO}_2}^0$	0.22 ²²	1.15	0.4
4	$\Delta G_{\text{HCOOH}}^0 - \Delta G_{\text{HCOO}_{\text{ad}}}^0$	−0.54 ²²	1.04	0.3
5	$\Delta G_{\text{H}_{\text{ad}}}^0$	−0.44 ²²	1.15 ¹⁰	0.5
6	$-\Delta G_{\text{H}_{\text{ad}}}^0$	0.44 ²²	1.31 ¹⁰	0.3

$$j_{\text{CO}} = 2e\rho v_2 \quad (15)$$

$$j_{\text{HCOOH}} = 2e\rho v_4 \quad (16)$$

$$j_{\text{H}_2} = 2e\rho v_6 \quad (17)$$

$$j_{\text{CO}_2} = j_{\text{CO}} + j_{\text{HCOOH}} \quad (18)$$

$$j_{\text{OH}^-} = -(j_{\text{CO}} + j_{\text{HCOOH}} + j_{\text{H}_2}) \quad (19)$$

with ρ the number density of active sites at Ag(110) and $e\rho = 0.68 \text{ C/m}^2$ is used in this model.¹⁰ Other parameters of the microkinetic model are listed in Tables 1 and 2, including the sources that they have been extracted from.

Table 2. Lateral Interaction Coefficients, ξ_{X_j, X_i} (eV)²²

X_i	X_j	
	HCOO_{ad}	H_{ad}
COOH_{ad}	0.2	1.2
HCOO_{ad}	0.5	0.4
H_{ad}	0.45	0.37

E_1^{eq} and E_2^{eq} have been calculated using DFT calculations in ref 23. E_3^{eq} , E_4^{eq} , E_5^{eq} , and E_6^{eq} have been obtained from the DFT studies in ref 22. For the CO pathway, β_1 and β_2 are set to the common value of 0.5. The activation barrier of step 1 in 0.1 M KHCO_3 (pH = 6.8) solution is determined to be 0.43 eV at −1.0 V vs RHE,¹⁰ and we have $G_{a,1}^{\text{eq}} = 0.43 - \beta_1 (-1.0 - 0.059 \times 6.8 - E_1^{\text{eq}}) = 0.53 \text{ eV}$. The activation barrier of step 2 is calculated to be 0.7 eV at −0.11 V vs RHE for Ag(111) at pH = 14,¹¹ and we have $G_{a,2}^{\text{eq}} = 0.7 - \beta_2 (-0.11 - 0.059 \times 14 - E_2^{\text{eq}}) = 1.4 \text{ eV}$.

There is little information for the HCOOH pathway at Ag because HCOOH is only a side product. Therefore, $G_{a,3}^{\text{eq}}$, $G_{a,4}^{\text{eq}}$, β_3 , and β_4 are fitted from the experimental data. For the H_2 pathway, DFT results show the activation barriers of the Volmer step and the Heyrovsky step as 0.52 and 0.72 eV at −1.0 V vs RHE at pH = 6.8, respectively,¹⁰ and we have $G_{a,5}^{\text{eq}} = 1.01 \text{ eV}$ and $G_{a,6}^{\text{eq}} = 1.27 \text{ eV}$. β_5 and β_6 are fitted to 0.5 and 0.3, respectively. The lateral interaction coefficients $\xi_{\text{HCOO}_{\text{ad}}, \text{COOH}_{\text{ad}}}$, $\xi_{\text{HCOO}_{\text{ad}}, \text{HCOO}_{\text{ad}}}$, $\xi_{\text{HCOO}_{\text{ad}}, \text{H}_{\text{ad}}}$, and $\xi_{\text{H}_{\text{ad}}, \text{COOH}_{\text{ad}}}$ have been taken from ref 22, assuming that the changes of binding energies due to lateral interactions are linearly related to the coverages. $\xi_{\text{H}_{\text{ad}}, \text{HCOO}_{\text{ad}}}$ and $\xi_{\text{H}_{\text{ad}}, \text{H}_{\text{ad}}}$ are fitting parameters. The energetic parameters are allowed to vary within 0.2 eV around their base values, considering the uncertainty associated with DFT calculations of reaction and transition-state energies.³⁴ Sensitivity analyses of fitting parameters, $G_{a,3}^{\text{eq}}$, $G_{a,4}^{\text{eq}}$, $\xi_{\text{H}_{\text{ad}}, \text{HCOO}_{\text{ad}}}$,

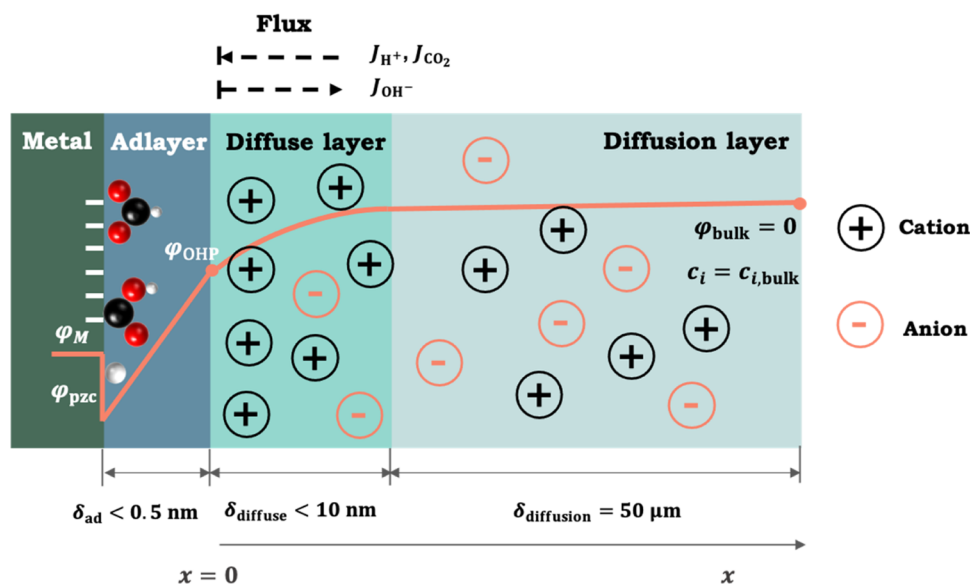


Figure 1. Schematic illustration of the model system. Three zones in the EDL are distinguished: adlayer, diffuse layer, and diffusion layer. The orange line is an illustrative potential profile for the case of negative surface charge, with φ_{pzc} and φ_{bulk} the potential of zero charge and bulk potential, respectively. δ_{ad} , δ_{diffuse} , and $\delta_{\text{diffusion}}$ are the thicknesses of space between the metal surface and the adsorbate layer, diffuse layer, and diffusion layer, respectively. Fluxes at the reaction plane (OHP) are indicated.

$\xi_{\text{H}_{2\text{O}}, \text{H}_{2\text{O}}}$, β_1 , β_2 , β_3 , β_4 , β_5 , and β_6 , are provided in the SI (Supplementary Note 3). To perform these analyses, we have varied the values of specific parameters in their feasible ranges while keeping all other parameters constant and then calculated the partial current densities at $\varphi_{\text{M}} = -1.2$ V and pH = 6.8. The high sensitivity of model performance to these parameters implies a high confidence of fitted parameters.

Mass Transport Model. The model system is shown in Figure 1. The hydrodynamic boundary layer thickness at the cathode surface was determined to be 50 μm according to the diffusion-limited current of ferricyanide reduction.²³ The dependence of the CO partial current density on the boundary layer thickness is depicted in Figure S2. The reaction plane (OHP) is located at $x = 0$. Outside the OHP resides the boundary layer, which includes the diffuse layer and the diffusion layer. In the diffuse layer, electrostatic interactions dominate over thermal motion, breaking the electroneutrality condition. The thickness of the diffuse layer is generally lower than 10 nm, 3 orders of magnitude smaller than that of the diffusion layer. We consider multicomponent mass transport including CO_2 , HCO_3^- , CO_3^{2-} , OH^- , H^+ , and K^+ .

The transport of species in the boundary layer is described by the modified Poisson–Nernst–Planck (PNP) theory, which takes into account steric effects.^{35,36} The Nernst–Planck equation is used to model the mass transport of species

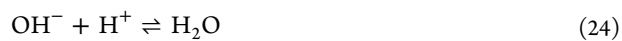
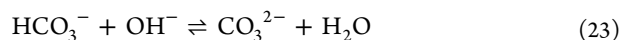
$$\frac{\partial c_i}{\partial t} = -\nabla \cdot J_i + R_i \quad (20)$$

where c_i is the concentration of species i , J_i is the flux of species i , and R_i is the rate of production of species i due to homogeneous reactions. The flux is given by

$$J_i = -D_i \left(\left(1 - \sum_{j \neq i} N_A a_j^3 c_j \right) \frac{\partial c_i}{\partial x} + c_i \sum_{j \neq i} N_A a_j^3 \frac{\partial c_j}{\partial x} + \frac{z_i F}{RT} c_i \left(1 - \sum_j N_A a_j^3 c_j \right) \frac{\partial \varphi}{\partial x} \right) \quad (21)$$

where D_i is the diffusion coefficient of species i , N_A is Avogadro's constant, a_j is the effective diameter of solvated species j , z_i is the charge number of species i , F is Faraday's constant, R is the gas constant, and φ is the electric potential.

The following homogeneous reactions in solution are considered



The values of rate constants of reactions 22–24 and the expressions for R_i can be found in the SI.

The Nernst–Planck equation is complemented by the Poisson equation

$$-\nabla \cdot (\epsilon_s \nabla \varphi) = F \sum_i z_i c_i \quad (25)$$

where ϵ_s is the permittivity of the electrolyte.

At steady state, $\frac{\partial c_i}{\partial t} = 0$, we have

$$\frac{\partial^2 C_i}{\partial X^2} = \frac{1}{\left(1 - \sum_{j \neq i} \gamma_j C_j\right)} \left(-R_i \frac{\lambda_D^2}{D_i} - C_i \sum_{j \neq i} \gamma_j \frac{\partial^2 C_j}{\partial X^2} + z_i C_i \frac{\partial \phi}{\partial X} \sum_j \gamma_j \frac{\partial C_j}{\partial X} - z_i \left(1 - \sum_j \gamma_j C_j\right) \left(\frac{\partial C_i}{\partial X} \frac{\partial \phi}{\partial X} + C_i \frac{\partial^2 \phi}{\partial X^2} \right) \right) \quad (26)$$

$$\frac{\partial^2 \phi}{\partial X^2} = -\frac{\sum z_i C_i c_0}{2 c_s} \quad (27)$$

where $C_i = c_i/c_0$ is the dimensionless concentration of species i , with $c_0 = 1$ M the reference concentration, X is the dimensionless spatial coordinate referenced to the Debye length $\lambda_D = \sqrt{\epsilon_s RT/2F^2 c_s}$, with c_s the solution concentration, $\gamma_j = N_A a_j^3 c_0$ is the size factor of species j , and $\phi = F\varphi/RT$ is the dimensionless potential. In this work, only the steric effect of K^+ is considered because the metal is negatively charged and K^+ is the counterion in the EDL. That is to say, we assume $\gamma_j C_j = 0$ for CO_2 , HCO_3^- , CO_3^{2-} , OH^- , and H^+ .

Next, we describe the boundary conditions to solve eqs 26 and 27. As shown in Figure 1 (right), the concentration is always equal to the bulk concentration, namely, $C_i = C_{i,bulk}$. The potential there is taken as the reference, $\varphi_{bulk} = 0$. The left side, $X = 0$, is located at the OHP, where reactions occur. The dimensionless flux of species i at $X = 0$ is given by

$$J_i = -D_i \left(\left(1 - \sum_{j \neq i} \gamma_j C_j\right) \frac{\partial C_i}{\partial X} \Big|_{X=0} + C_i \sum_{j \neq i} \gamma_j \frac{\partial C_j}{\partial X} \Big|_{X=0} + z_i C_i \left(1 - \sum_j \gamma_j C_j\right) \frac{\partial \phi}{\partial X} \Big|_{X=0} \right) = \frac{\lambda_D}{c_0} \frac{j_i}{n_{e,i} F} \quad (28)$$

where j_i is the partial current density that consumes ($j_i > 0$) or generates ($j_i < 0$) species i and $n_{e,i}$ is the number of electrons involved in the reaction. We have $n_{e,CO_2} = 2$, $n_{e,OH^-} = n_{e,H^+} = 1$, and $J_i = 0$ for other buffer species; j_i is calculated using the microkinetic model. The boundary condition of potential is given by^{21,37}

$$\sigma_M = -\epsilon_s \frac{\partial \varphi}{\partial X} \Big|_{X=0} = \frac{\epsilon_{OHP}}{\delta_{OHP}} \left(\varphi_M - \varphi_{pzc} - \varphi_{OHP} - \frac{\mu_X}{\epsilon_{OHP}} \right) \quad (29)$$

where σ_M is the free surface charge density, ϵ_{OHP} is the permittivity of the space between the metal and the OHP and is assumed to be uniform, δ_{OHP} is the distance from the metal to the OHP, and μ_X is the interfacial adsorbate dipole moment^{38,39}

$$\mu_X = e\rho(\theta_{COOH_{ad}} \zeta_{COOH_{ad}} + \theta_{HCOO_{ad}} \zeta_{HCOO_{ad}} + \theta_{H_{ad}} \zeta_{H_{ad}}) \delta_{ad} \quad (30)$$

with $\zeta_{COOH_{ad}}$, $\zeta_{HCOO_{ad}}$, and $\zeta_{H_{ad}}$ the net electron numbers of $COOH_{ad}$, $HCOO_{ad}$, and H_{ad} , respectively, and δ_{ad} the thickness of the space between the metal surface and the

adsorbate layer. $\theta_{COOH_{ad}} \zeta_{COOH_{ad}}$ can be neglected because $\theta_{COOH_{ad}} \approx 0$. The parameters of the EDL are listed in Table 3. The detailed parameters for mass transport, including bulk concentrations, diffusion coefficients, and effective solvated diameters, can be found in Table S2.

Table 3. Parameters of the EDL

item	category	value	note
$\zeta_{HCOO_{ad}}$	net charge number per adsorbate	0.68	ref 22
$\zeta_{H_{ad}}$		0.25	
φ_{pzc}	potential of zero charge	−0.73 V (SHE)	ref 23
ϵ_s	permittivity of the electrolyte solution	78.5 ϵ_0	ϵ_0 is the permittivity of vacuum
ϵ_{OHP}	permittivity of the space between the metal and the OHP	6 ϵ_0	ref 35
δ_{OHP}	distance from the metal to the OHP	0.275 nm	diameter of H_2O
δ_{ad}	thickness of the space between the metal surface and the adsorbate layer	0.2 nm	bond length of Pt–OH _{ad} ⁴⁰

Numerical Solution. The model was solved in Matlab iteratively. Given the initial current densities and coverages at a specific applied potential, the potential distribution and the concentration distributions in the solution phase can be obtained from the mass transport model. The calculated OHP potential and reactant concentrations were then used in the microkinetic model to calculate new values of current densities and coverages. The cycle iterates until the current densities are converged. The convergence criterion is set to be 10^{-3} .

REVEALING THE IMPACT OF THE LOCAL REACTION ENVIRONMENT

In the following, we first validate the model by comparing simulation results with experimental data. We then present a detailed mechanistic analysis on the bell-shaped polarization curve and the origins of potential dependencies in Tafel slopes.

Model–Experiment Comparison. Figure 2 shows the simulated CO partial current density in the potential range between −0.3 and −1.4 V. Experimental data from Clark et al.,²³ Hoshi et al.,²⁴ Hatsukade et al.,²⁶ and Singh et al.⁴¹ are closely reproduced by our model. The experimentally observed increasing Tafel slope with overpotential is captured. Specifically, the CO partial current density increases with overpotential when $\varphi_M > -1.25$ V and decreases when $\varphi_M < -1.25$ V, resulting in the peculiar bell shape. The simulated partial current densities of HCOOH and H_2 are shown in Figure S8. A mechanistic explanation of the bell shape is to be given in the following section.

Origins of the Bell-Shaped Curve. The maximum current density is only about 5 mA/cm² at $\varphi_M = -1.25$ V, which is much smaller than the diffusion-limited current density that is estimated as ~ 20 mA/cm² using the mass transport model.¹⁰ As shown in Figure 3a, the partial current density of CO_2 , $j_{CO_2} = j_{CO} + j_{HCOOH}$, decreases at high overpotentials, implying that the decreasing trend cannot be explained by the increasing consumption rate of CO_2 .

According to eqs 1, 4, and 5, we have

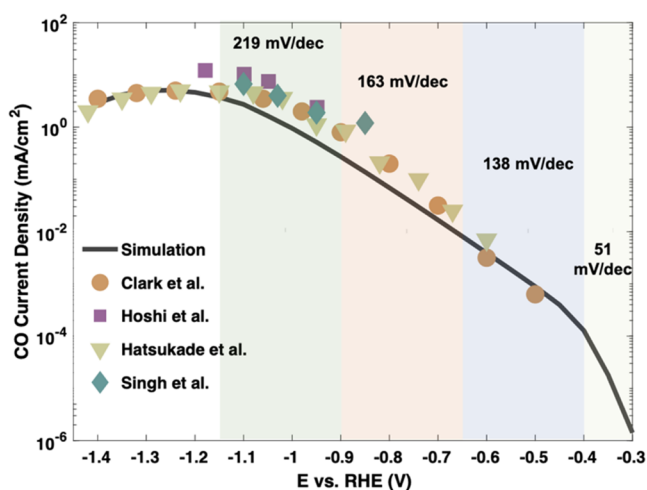


Figure 2. Model–experiment comparison in terms of the CO partial current density. Experiment data are taken from Clark et al.,²³ Hoshi et al.,²⁴ Hatsukade et al.,²⁶ and Singh et al.⁴¹ Data were obtained on Ag(110) in refs 23 and 24, and polycrystalline Ag in refs 26 and 41, in 0.1 M KHCO₃ solution. The Tafel slopes were calculated in different potential ranges as marked by different background colors.

$$\theta_{\text{COOH}_{\text{ad}}} = \frac{k_1 c_{\text{CO}_2}^{\text{OHP}} \theta_0}{k_{-1} c_{\text{OH}^-}^{\text{OHP}} + k_2} \quad (31)$$

$$\frac{1}{\text{TOF}} = \frac{1}{k_2 \theta_{\text{COOH}_{\text{ad}}}} = \frac{1}{k_1 c_{\text{CO}_2}^{\text{OHP}} \theta_0} + \frac{c_{\text{OH}^-}^{\text{OHP}}}{K_1 k_2 c_{\text{CO}_2}^{\text{OHP}} \theta_0} \quad (32)$$

with $K_1 = k_1/k_{-1}$ being the equilibrium constant of step 1. In eq 32, $1/\text{TOF}$ represents the effective resistance of CO₂ RR to CO, which consists of two terms. Therefore, the activity of CO₂ RR to CO can be represented as a series of resistances. In the context of a serial resistor network, the notion of a rate-determining term (RDT) becomes meaningful.^{33,42}

As shown in Figure 3b, $\frac{c_{\text{OH}^-}^{\text{OHP}}}{K_1 k_2 c_{\text{CO}_2}^{\text{OHP}} \theta_0}$ is the RDT when $\varphi_M > -0.5$ V, and $\frac{1}{k_1 c_{\text{CO}_2}^{\text{OHP}} \theta_0}$ is the RDT when $\varphi_M < -0.5$ V. Therefore, the increasing current density at $\varphi_M > -0.5$ V is due to the decrease of $\frac{c_{\text{OH}^-}^{\text{OHP}}}{K_1 k_2 c_{\text{CO}_2}^{\text{OHP}} \theta_0}$. $\frac{1}{k_1 c_{\text{CO}_2}^{\text{OHP}} \theta_0}$ decreases with overpotential when -1.25 V $< \varphi_M < -0.5$ V and increases when $\varphi_M < -1.25$ V, resulting in the nonmonotonic current density. To understand the nonmonotonic behavior, we need to analyze the potential dependence of k_1 , K_1 , k_2 , $c_{\text{CO}_2}^{\text{OHP}}$, $c_{\text{OH}^-}^{\text{OHP}}$, and θ_0 .

As shown in Figure 3c, k_1 deviates from the Tafel equation, $k_i = k_i^0 \exp\left(-\frac{\beta_i^{\text{FE}}}{RT}\right)$. Two factors are responsible for this deviation: the surface charging effects and lateral adsorbate–adsorbate interactions. φ_{OHP} is negative due to negative σ_M (Figure 3d), and decreases with overpotential following the surface charging relation, as presented in Figure S9. Consequently, the driving force of interfacial charge transfer, defined as $-(\varphi_M - \varphi_{\text{OHP}} - E_i^{\text{eq}})$, is lower than $-(\varphi_M - E_i^{\text{eq}})$. This effect is essentially a Frumkin correction. DFT calculations have shown that H_{ad} repels COOH_{ad} more than HCOO_{ad}.²² With increasing overpotential, HCOO_{ad} is replaced by H_{ad} (Figure 3e), inhibiting the formation of COOH_{ad} to a greater extent. When $\varphi_M < -1.25$ V, $G_{\text{a},1}$ increases anomalously with overpotential because ΔG_1

increases due to lateral adsorbate interactions (eqs 11 and 13), resulting in the decrease of k_1 . K_1 and k_2 increase monotonically when $\varphi_M > -0.5$ V, as shown in Figures S10 and S11.

As shown in Figure 3e, $\theta_{\text{HCOO}_{\text{ad}}}$ is dominant over $\theta_{\text{COOH}_{\text{ad}}}$ and $\theta_{\text{H}_{\text{ad}}}$ when $\varphi_M > -1.1$ V and decreases with overpotential. $\theta_{\text{COOH}_{\text{ad}}}$ is nearly zero in the whole potential range. In addition, we find $\theta_{\text{H}_{\text{ad}}} \approx 0$ when $\varphi_M > -1.1$ V and $\theta_{\text{H}_{\text{ad}}}$ increases with overpotential. θ_0 remains almost constant due to the balance between $\theta_{\text{HCOO}_{\text{ad}}}$ and $\theta_{\text{H}_{\text{ad}}}$.

$c_{\text{CO}_2}^{\text{OHP}}$ decreases monotonically with overpotential, as shown in Figure 3f. It should be noted that $c_{\text{CO}_2}^{\text{OHP}}$ is influenced not only by the mass transport of CO₂ but also by the surface charge density. The magnitude of negative σ_M increases with overpotential (Figure 3d). Therefore, the concentration of K⁺ at the OHP dramatically increases due to electrostatic attraction (Figure S12). K⁺ occupies most of the space near the electrode surface, thus repelling CO₂.²¹ $c_{\text{OH}^-}^{\text{OHP}}$ decreases slowly for $\varphi_M > -0.6$ V due to the electrostatic repulsion; it increases for $\varphi_M < -0.6$ V due to the increasing generation rate of OH[−] (see j_{OH^-} in Figure S13), as shown in Figure S14. It should be noted that the increase in $c_{\text{OH}^-}^{\text{OHP}}$ also decreases $c_{\text{CO}_2}^{\text{OHP}}$ through the homogenous reaction in eq 22.

Combined, when $\varphi_M > -0.5$ V, $c_{\text{CO}_2}^{\text{OHP}}$, $c_{\text{OH}^-}^{\text{OHP}}$, and θ_0 remain nearly constant, the dominant term in $\frac{c_{\text{OH}^-}^{\text{OHP}}}{K_1 k_2 c_{\text{CO}_2}^{\text{OHP}} \theta_0}$ is $K_1 k_2$, which increases monotonically with overpotential, leading to the decrease of $\frac{c_{\text{OH}^-}^{\text{OHP}}}{K_1 k_2 c_{\text{CO}_2}^{\text{OHP}} \theta_0}$; when -1.25 V $< \varphi_M < -0.5$ V, the increase of k_1 dominates over the decrease of $c_{\text{CO}_2}^{\text{OHP}}$, causing the decrease of $\frac{1}{k_1 c_{\text{CO}_2}^{\text{OHP}} \theta_0}$; when $\varphi_M < -1.25$ V, both k_1 and $c_{\text{CO}_2}^{\text{OHP}}$ decrease, resulting in the increase of $\frac{1}{k_1 c_{\text{CO}_2}^{\text{OHP}} \theta_0}$.

In conclusion, the activity of the CO₂ RR to CO is not only determined by the intrinsic kinetics that increases monotonically with overpotential but also by the LRE. The LRE is determined by the interplay between the mass transport effects that decrease the CO₂ concentration in the OHP, the surface charging effects that decrease the driving force of interfacial charge transfer and block CO₂ transport, and the lateral interactions between adsorbates that inhibit the adsorption of COOH_{ad}. Specifically, the intrinsic kinetics dominates when $\varphi_M > -1.25$ V, resulting in the decrease of $\frac{c_{\text{OH}^-}^{\text{OHP}}}{K_1 k_2 c_{\text{CO}_2}^{\text{OHP}} \theta_0}$ and $\frac{1}{k_1 c_{\text{CO}_2}^{\text{OHP}} \theta_0}$.

As a result, the CO current density increases with overpotential in this potential range. When -1.4 V $< \varphi_M < -1.25$ V, $c_{\text{CO}_2}^{\text{OHP}}$ decreases, and the repulsive effect on COOH_{ad} from lateral interactions becomes stronger, causing the anomalous decrease of the CO current density.

It has been proposed that the decrease of j_{CO} on Ag is mainly caused by the enhanced rate of hydrogen evolution, which generates OH[−] and thus decreases CO₂ concentration.⁴³ We compare the distribution of C_{CO_2} at -1.25 and -1.4 V using experimental current densities as fluxes (Figure S15). It can be seen that $c_{\text{CO}_2}^{\text{OHP}}$ at -1.4 V is about 40% $c_{\text{CO}_2}^{\text{OHP}}$ at -1.25 V. If the lateral interactions are neglected, k_1 at -1.25 V should be only about 5% of k_1 at -1.4 V according to the Butler–Volmer equation. Based on this assessment, it is expected that $k_1 c_{\text{CO}_2}^{\text{OHP}}$

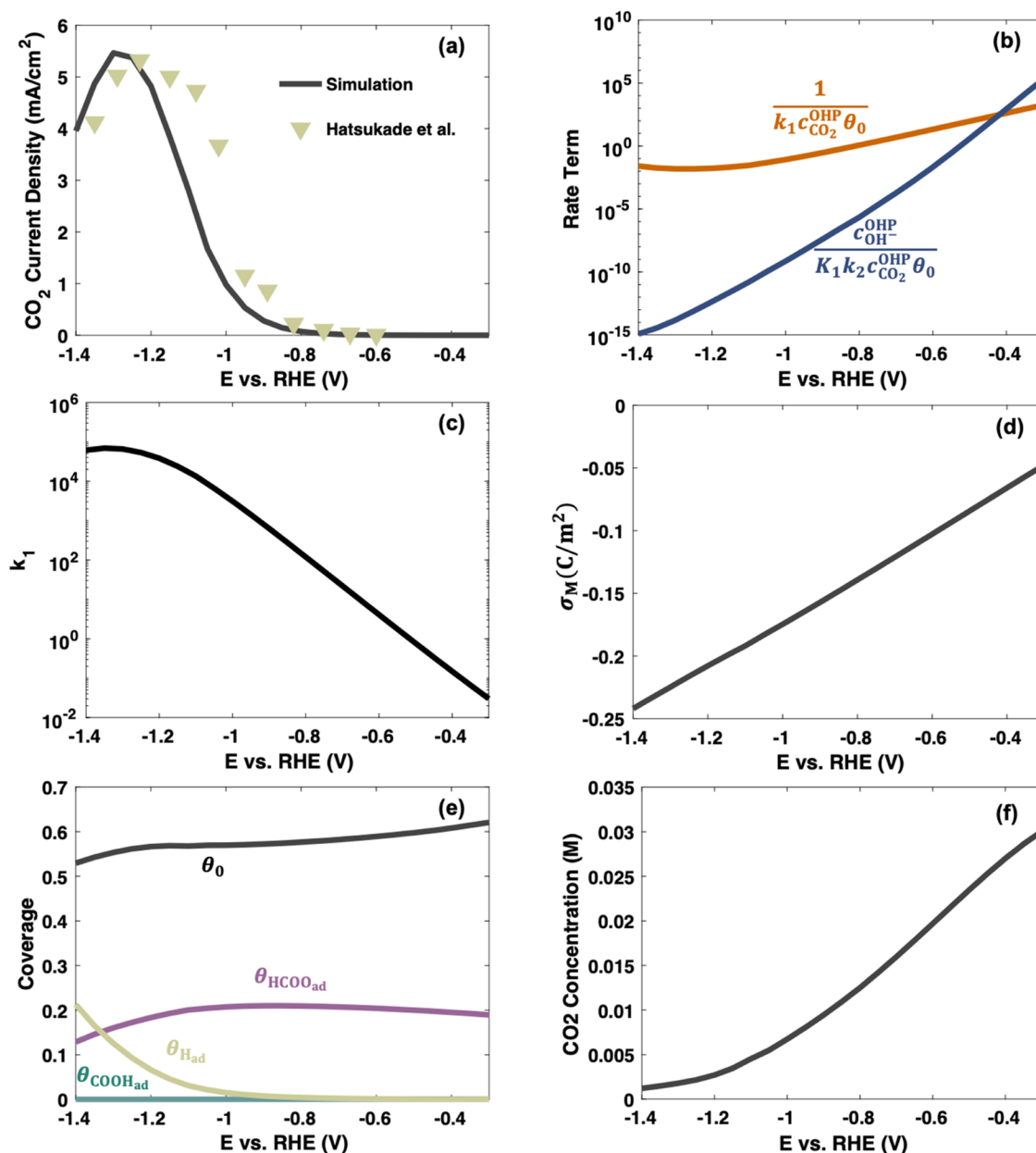


Figure 3. (a) Model–experiment comparison in terms of the CO_2 partial current density; experimental data are taken from Hatsukade et al.²⁶ (b) Rate-determining terms of the CO partial current density. (c) Forward rate constant of step 1, k_1 . (d) Surface charge density. (e) Coverages of COOH_{ad} , HCOO_{ad} , H_{ad} , and free sites. (f) CO_2 concentration at the OHP.

increases with overpotential. Therefore, only considering the decrease of CO_2 concentration is insufficient to rationalize the decrease of j_{CO} with increasing overpotential bringing into play lateral interactions as another possible (and, in our understanding, likely) origin of the observed trend. In this context, it should be noted that HCOO_{ad} was detected by surface-enhanced Raman spectroscopy,²² whereas, interestingly, H_{ad} was detected by infrared spectroscopy in the absence of CO_2 and disappeared when CO_2 was introduced.³¹ Furthermore, it was observed that the HER was severely suppressed in CO_2 -saturated solution.²³ These observations together suggest a significant impact of interactions between adsorbates.

Origin of the Potential-Dependent Tafel Slope. As shown in Figure 2, the model gives $b = 51$ mV/dec (close to 59 mV/dec) when $\varphi_M < -0.4$ V, and $b > 118$ mV/dec when -0.4 V $< \varphi_M < -1.2$ V, consistent with experimental measurements

on bulk Ag,⁹ nanostructured Ag,⁸ polycrystalline Au,²⁷ and oxide-derived Au.⁴⁴ To explain the potential-dependent Tafel slope, we first explore the intrinsic kinetics of the CO pathway. This means that we neglect for the moment the competitive reactions, mass transport, and surface charging effects. In this case, the analytical expression for $\theta_{\text{COOH}_{\text{ad}}}$ can be obtained as

$$\theta_{\text{COOH}_{\text{ad}}} = \frac{k_1 c_{\text{CO}_2}}{k_1 c_{\text{CO}_2} + k_{-1} c_{\text{OH}^-} + k_2} \quad (33)$$

Then, we have

$$\frac{1}{\text{TOF}} = \frac{1}{k_2 \theta_{\text{COOH}_{\text{ad}}}} = \frac{1}{k_2} + \frac{1}{k_1 c_{\text{CO}_2}} + \frac{1}{K_1 k_2} \frac{c_{\text{OH}^-}}{c_{\text{CO}_2}} \quad (34)$$

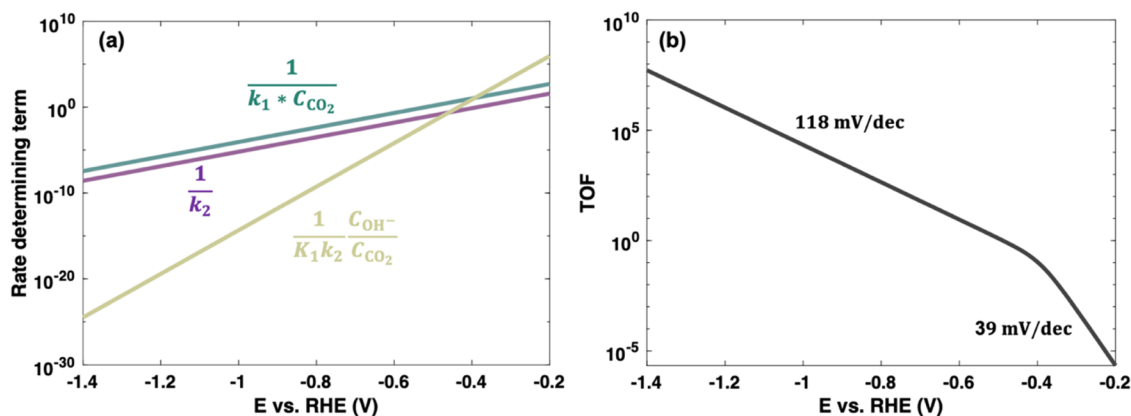


Figure 4. (a) Rate-determining terms and (b) intrinsic activity–potential relation of the CO₂ RR to CO. The rate constants are calculated using $k_{\pm i} = \frac{k_{\pm i}^0}{h} \exp\left(-\frac{C_{\pm i}^{\text{eq}} \pm \beta_i F(\varphi_M - E_i^{\text{eq}})}{RT}\right)$, with parameters taken from Table 1. The concentrations C_{CO_2} and C_{OH^-} are equal to their bulk concentrations.

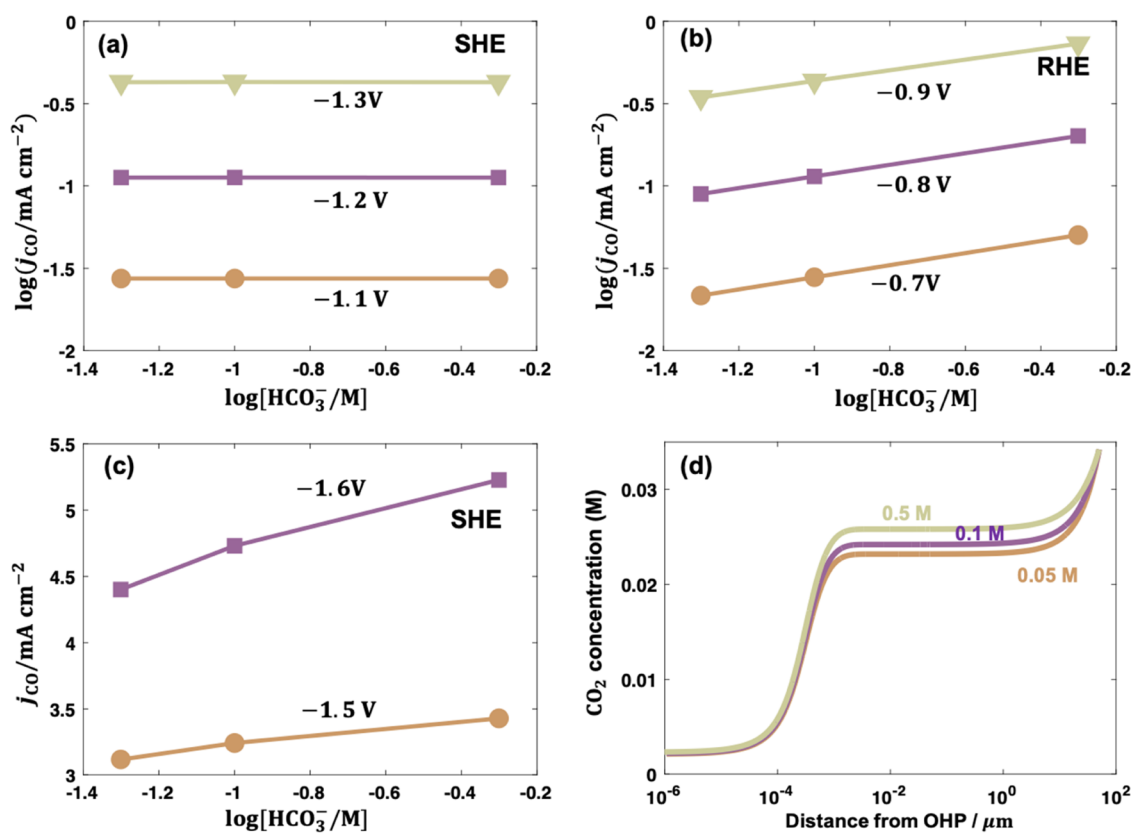


Figure 5. Bicarbonate concentration dependence of the CO partial current density at (a) -1.1 , -1.2 , -1.3 V vs SHE; (b) at -0.7 , -0.8 , -0.9 V vs RHE; and (c) at -1.5 and -1.6 V vs SHE. (d) Concentration distributions of CO₂ in solutions with 0.05, 0.1, and 0.5 M bicarbonate at -1.6 V vs SHE.

Figure 4a displays RDTs as a function of potential. When $\varphi_M > -0.4$ V, $\frac{1}{K_1 k_2 C_{\text{CO}_2}}$ is the RDT, and $b = \frac{2.3RT}{(1 + \beta_2)F} = 39$ mV/dec, as shown in Figure 4b. When $\varphi_M < -0.4$ V, $\frac{1}{k_1 C_{\text{CO}_2}}$ is the RDT, and $b = \frac{2.3RT}{\beta_1 F} = 118$ mV/dec. A more general analysis of the Tafel slope of multielectron reactions can be found in ref 42.

Starting from the intrinsic Tafel slopes shown in Figure 4b, we add complexity to the analysis by considering the impact of the LRE. When -1.25 V $< \varphi_M < -0.4$ V, both j_{CO_2} and negative σ_M increase with increasing overpotential, as shown in Figure 3a,d, leading to $b > 118$ mV/dec. When $\varphi_M > -0.4$ V,

j_{CO_2} is very small and $\theta_{\text{HCO}_3^-}$, $\theta_{\text{H}_2\text{O}}$, and θ_0 remain almost constant (Figure 3a,e), indicating that the competitive reactions and mass transport effects are unimportant in this potential range. Instead, the primary factor controlling the Tafel slope is the surface charging relation, which decreases the driving force and $C_{\text{CO}_2}^{\text{OHP}}$. Thus, the Tafel slope increases from 39 to 51 mV/dec (close to 59 mV/dec). It should be noted that 39 and 59 mV/dec refer to different rate-determining steps in the Tafel analysis. Consequently, it is necessary to consider the LRE when deciphering the reaction mechanisms with Tafel analysis.

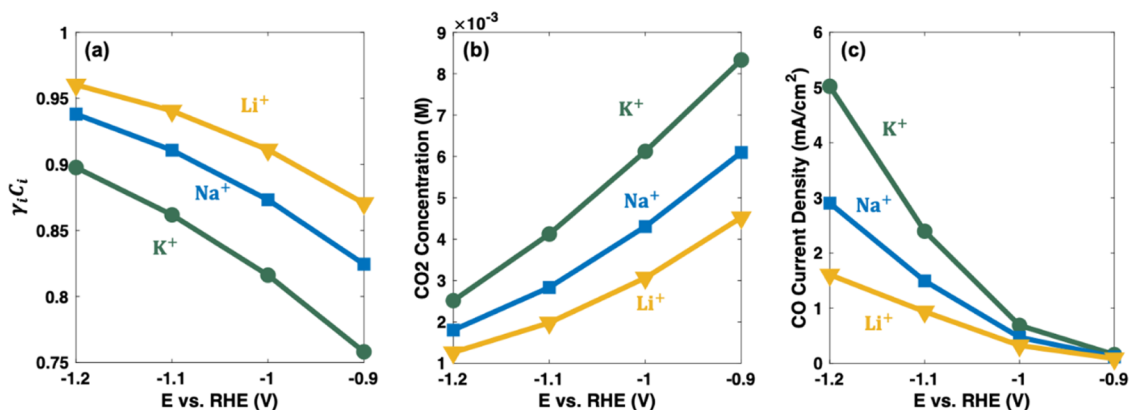


Figure 6. (a) Intensity of the steric effect of cations, (b) CO₂ concentrations at OHP, and (c) CO partial current densities in 0.1 M KHCO₃/NaHCO₃/LiHCO₃ solutions.

TUNING THE LOCATION REACTION ENVIRONMENT

In this section, we demonstrate how the local reaction environment can be tuned by varying the bicarbonate concentration, the type of electrolyte cations, and the CO₂ pressure.

Role of Bicarbonate. The bicarbonate (HCO₃[−]) is involved in the homogeneous reactions in eqs 22 and 23. Therefore, we can tune the LRE by varying the concentration of HCO₃[−], $c_{HCO_3^-}$. As the solution pH changes with $c_{HCO_3^-}$, the influence of $c_{HCO_3^-}$ is different on SHE and RHE scales. Let us change $c_{HCO_3^-}$ from 0.05 to 0.5 M at fixed ionic strength and K⁺ concentration by adding KClO₄. For this case, the pH shifts from 6.5 to 7.5. If the electrode potential is referenced to the SHE scale, j_{CO} should be independent of $c_{HCO_3^-}$ when the mass transport effects are insignificant because HCO₃[−] is not involved in the reaction mechanism (Steps 1–6). If the electrode potential is referenced to the RHE scale, the driving force, defined as $-(\varphi_{M,SHE} - E_{i,SHE}^{eq})$, will increase by an amount of $\frac{RT \ln 10}{F} = 59$ mV (neglecting the surface charging effect for the moment, namely, $\varphi_{OHP} = 0$). As discussed in the previous section, $\frac{1}{K_i k_2} \frac{C_{OH^-}}{C_{CO_2}}$ is the RDT for $\varphi_M > -0.4$ V, the dependence of j_{CO} on bicarbonate concentration, denoted as $b_{HCO_3^-}$, is 0.5; $\frac{1}{k_1 C_{CO_2}}$ is the RDT for $\varphi_M < -0.4$ V, resulting also in $b_{HCO_3^-} = 0.5$. We calculate $b_{HCO_3^-}$ at −1.1, −1.2, and −1.3 V vs SHE, all being 0, as shown in Figure 5a. When the RHE scale is used, $b_{HCO_3^-} \approx 0.4$ is obtained, regardless of the overpotential, as shown in Figure 5b. $b_{HCO_3^-}$ is smaller than 0.5 because σ_M becomes more negative with $c_{HCO_3^-}$ due to the pH increase, and the mass transport effects grow with increasing j_{CO} .

In experimental studies, both $b_{HCO_3^-} = 0.5$ ^{8,27} and $b_{HCO_3^-} = 0$ ⁴⁵ have been reported, leading to different conclusions on the role of bicarbonate. Here, we clarify that the different experimental values of $b_{HCO_3^-}$ are caused by the use of different potential scales. It should also be noted that $b_{HCO_3^-} \approx 1$ was observed on oxide-derived Au nanoparticles,⁴⁴ and the polycrystalline Au.²⁷ This abnormal value of $b_{HCO_3^-} \approx 1$ is related to the unusual experimental conditions. In ref 44,

$b_{HCO_3^-}$ is determined at potentials with severe mass transport limitations. In addition, phosphate, which has been shown to inhibit the reaction,⁴⁵ was used as a buffer to maintain the ionic strength in ref 27.

However, the higher $c_{HCO_3^-}$ can increase j_{CO} on the SHE scale when the mass transport effects are significant, as shown in Figure 5c. This enhancement can be attributed to the buffering capacity of bicarbonate, which can maintain the local pH (Figure S16), and consequently increase the local CO₂ concentration by inhibiting the homogeneous reaction of eq 22, as shown in Figure 5d.

In conclusion, $c_{HCO_3^-}$ affects the LRE by changing the pH and buffering capacity of the solution. On the SHE scale, j_{CO} is independent of $c_{HCO_3^-}$, when mass transport effects are insignificant since HCO₃[−] is not the direct reactant, while it increases with $c_{HCO_3^-}$, when mass transport effects are significant because of the buffering capacity of HCO₃[−]. On the RHE scale, $b_{HCO_3^-} \approx 0.5$ is obtained due to the pH shift.

Cation Effects. The LRE can also be tuned using different electrolyte cations. For nonspecifically adsorbing cations, they are characterized by the effective size, the diffusion coefficient, and the charge number. In this section, we considered three cations, K⁺, Na⁺, and Li⁺, with $a_{K^+} < a_{Na^+} < a_{Li^+}$, considering their solvation shells.⁴⁶ The electrolyte solutions are 0.1 M KHCO₃/NaHCO₃/LiHCO₃. As shown in Figure 6a, the intensity of the steric effect of cations, $\gamma_i C_i$, follows the order of $\gamma_{K^+} C_{K^+} < \gamma_{Na^+} C_{Na^+} < \gamma_{Li^+} C_{Li^+}$, consistent with the order of solvated ion size. A larger $\gamma_i C_i$ means a stronger steric effect, leading to a decreased $c_{CO_2}^{OHP}$, as shown in Figure 6b. Consequently, j_{CO} follows the order of $K^+ > Na^+ > Li^+$, Figure 6c, which is in line with experimental observations.⁴¹ The pH at OHP follows the order $K^+ > Na^+ > Li^+$, as shown in Figure S17, which is consistent with the results in ref 47. The cation size effect on j_{HCOOH} is similar to that on j_{CO} , as the two pathways share the same reactant CO₂ (Figure S18). However, j_{H_2} is not sensitive to the cation sizes of K⁺, Na⁺, and Li⁺ as the proton precursor is H₂O and the backward reaction of Step 5 can be neglected ($k_{-5}^{OHP} \ll k_5$). The results in Figure S18 are in agreement with experimental results.⁴¹ It should be noted that cation effects are multifaceted in electrocatalysis, including, for instance, hydrolysis,⁴¹ promoter,⁴⁸ and electric field effects.^{11,30} Our analysis emphasizes the steric effect. The

same cation overcrowding effect has recently also been applied to explain the cation effect on the oxygen evolution reaction.⁴⁹

Effects of CO₂ Pressure. CO₂ is involved not only in the electrochemical reactions (Steps 1–4), but also in the homogeneous reaction in eq 22. Therefore, varying the pressure of CO₂ will affect the LRE in two ways: changing the local CO₂ concentration and pH and modifying adsorbate coverages on the catalyst surface. Herein, we investigate the dependence of j_{CO} on CO₂ pressure (defined as b_{CO_2}) in 0.1 M KHCO₃ solution. For convenience, the SHE scale is used considering the shift of bulk pH with CO₂ pressure.

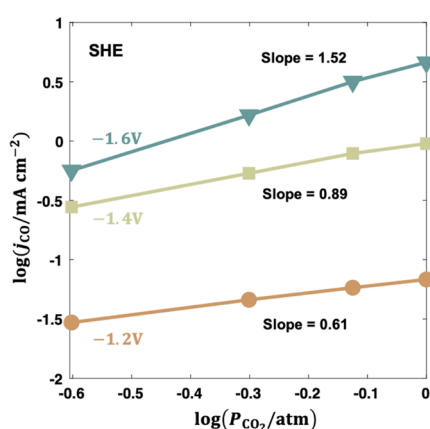


Figure 7. CO₂ partial pressure dependence of j_{CO} at -1.2, -1.4, and -1.6 V vs SHE.

As shown in Figure 7, we find that b_{CO_2} increases sequentially with overpotential, being <1 at -1.2 and -1.4 V and >1 at -1.6 V. The variation of b_{CO_2} with potential is caused by the influence of LRE. At low overpotentials, $\theta_{\text{H}_{\text{ad}}}$ is negligible, while the increase of CO₂ concentration promotes the adsorption of HCOO_{ad}. Thus, the increase of $\theta_{\text{HCOO}_{\text{ad}}}$ inhibits the CO pathway through site blocking effect and lateral interactions, leading to $b_{\text{CO}_2} < 1$. At high overpotentials, $\theta_{\text{H}_{\text{ad}}}$ is not negligible, the increase of $\theta_{\text{HCOO}_{\text{ad}}}$ can inhibit the adsorption of H_{ad}, which has a stronger repulsion effect to COOH_{ad} leading to $b_{\text{CO}_2} > 1$. The simulated b_{CO_2} shows good agreement with the experiment data at -1.2 V (RHE), as shown in Figure S19. However, b_{CO_2} at a specific overpotential is usually used as a mechanistic probe for the CO₂ RR. $b_{\text{CO}_2} \approx 0.5^8$ and $b_{\text{CO}_2} \approx 1^{27,50}$ have been reported in the literature, leading to different reaction mechanisms. Here, we caution not to use the observed b_{CO_2} as a probe of the reaction mechanism, and not to use $b_{\text{CO}_2} = 1$ to determine the reaction rate in kinetic modeling.

CONCLUSIONS

We developed a detailed transport-reaction model to unravel the influence of the local reaction environment on the CO₂RR at a Ag electrode. It accounts for the multistep kinetics, mass transport, and surface charge effects. Several important insights are gleaned from the model.

First, the model explains the bell-shaped CO partial current density caused by the transition between rate-determining terms. The intrinsic kinetics is dominant at low and medium overpotentials, resulting in the increase of activity. Based on our assessment of the CO₂ concentration at the OHP, the anomalous decrease of the CO partial current density at high overpotentials is unlikely to be attributable solely to the decrease of CO₂ concentration. However, a consistent explanation of the trend can be given if lateral interactions between HCOO_{ad}, COOH_{ad}, and H_{ad} are accounted for in the model. This, of course, does not exclude other explanations of the experimental trends so far not accounted for in the model. In addition, we show that the experimentally observed Tafel slope of 59 mV/dec at low overpotentials is a combined result of the intrinsic slope of 39 mV/dec and the surface charge effects, while the Tafel slope of >118 mV/dec at medium overpotentials is a combined result of the intrinsic slope 118 mV/dec, the surface charge effects, and the mass transport effects.

The local reaction environment was tuned by varying the bicarbonate concentration, the type of electrolyte cation, and the CO₂ pressure. We show that the bicarbonate is neither the direct reaction partner nor the main source of CO₂, but it can increase the local CO₂ concentration when the mass transport effects are significant by maintaining the local pH and inhibiting the homogeneous reaction of CO₂ to HCO₃⁻. The steric effect of cations is shown to increase with the solvated size of cations, resulting in the activity in the order of K⁺ > Na⁺ > Li⁺. Besides, the dependence of activity on the pressure of CO₂ was shown to change with overpotential. These results together stress the importance of the local reaction environment in understanding electrocatalytic reactions.

It should be noted that the model-based insights are specific to the system studied here, although the modeling approach is general. Therefore, words of caution are needed when applying the insights to other cases.

ASSOCIATED CONTENT

Supporting Information

The Supporting Information is available free of charge at <https://pubs.acs.org/doi/10.1021/acscatal.1c04791>.

H⁺ limiting current density; parameters of mass transport model; boundary layer thickness dependence of model performance; sensitivity analysis; model–experiment comparison in terms of HCOOH partial current density and H₂ partial current density; OH⁻ concentration at OHP; distribution of CO₂ concentration at -1.25 and -1.4 V; bicarbonate concentration effects on pH; and cation effects on pH, HCOOH, and H₂ partial current densities (PDF)

AUTHOR INFORMATION

Corresponding Author

Michael Eikerling – Theory and Computation of Energy Materials (IEK-13), Institute of Energy and Climate Research, Forschungszentrum Jülich GmbH, 52425 Jülich, Germany; Chair of Theory and Computation of Energy Materials, Faculty of Georesources and Materials Engineering, RWTH Aachen University, 52062 Aachen, Germany; orcid.org/0000-0002-0764-8948; Email: m.eikerling@fz-juelich.de

Authors

Xinwei Zhu – Theory and Computation of Energy Materials (IEK-13), Institute of Energy and Climate Research, Forschungszentrum Jülich GmbH, 52425 Jülich, Germany; Chair of Theory and Computation of Energy Materials, Faculty of Georesources and Materials Engineering, RWTH Aachen University, 52062 Aachen, Germany; orcid.org/0000-0002-4636-8893

Jun Huang – Theory and Computation of Energy Materials (IEK-13), Institute of Energy and Climate Research, Forschungszentrum Jülich GmbH, 52425 Jülich, Germany; Institute of Theoretical Chemistry, Ulm University, 89069 Ulm, Germany; orcid.org/0000-0002-1668-5361

Complete contact information is available at:
<https://pubs.acs.org/10.1021/acscatal.1c04791>

Notes

The authors declare no competing financial interest.

ACKNOWLEDGMENTS

M.E. acknowledges the financial support from Forschungszentrum Jülich GmbH. J.H. acknowledges the funding provided by the Alexander von Humboldt Foundation.

REFERENCES

- (1) *Electrochemical Reduction of Carbon Dioxide: Overcoming the Limitations of Photosynthesis*; Marken, F.; Fermin, D., Eds.; Energy and Environment Series; Royal Society of Chemistry: Cambridge, U.K., 2018.
- (2) *Modern Aspects of Electrochemistry*; Vayenas, C. G.; White, R. E.; Gamboa-Aldeco, M. E., Eds.; Springer: New York, 2008; Vol. 42.
- (3) Nitopi, S.; Bertheussen, E.; Scott, S. B.; Liu, X.; Engstfeld, A. K.; Horch, S.; Seger, B.; Stephens, I. E. L.; Chan, K.; Hahn, C.; Nørskov, J. K.; Jaramillo, T. F.; Chorkendorff, I. Progress and Perspectives of Electrochemical CO₂ Reduction on Copper in Aqueous Electrolyte. *Chem. Rev.* **2019**, *119*, 7610–7672.
- (4) Sebastián-Pascual, P.; Mezzavilla, S.; Stephens, I. E. L.; Escudero-Escribano, M. Structure-Sensitivity and Electrolyte Effects in CO₂ Electroreduction: From Model Studies to Applications. *ChemCatChem* **2019**, *11*, 3626–3645.
- (5) Kibria, M. G.; Edwards, J. P.; Gabardo, C. M.; Dinh, C.; Seifitokaldani, A.; Sinton, D.; Sargent, E. H. Electrochemical CO₂ Reduction into Chemical Feedstocks: From Mechanistic Electrocatalysis Models to System Design. *Adv. Mater.* **2019**, *31*, No. 1807166.
- (6) Feaster, J. T.; Shi, C.; Cave, E. R.; Hatsukade, T.; Abram, D. N.; Kuhl, K. P.; Hahn, C.; Nørskov, J. K.; Jaramillo, T. F. Understanding Selectivity for the Electrochemical Reduction of Carbon Dioxide to Formic Acid and Carbon Monoxide on Metal Electrodes. *ACS Catal.* **2017**, *7*, 4822–4827.
- (7) Hansen, H. A.; Varley, J. B.; Peterson, A. A.; Nørskov, J. K. Understanding Trends in the Electrocatalytic Activity of Metals and Enzymes for CO₂ Reduction to CO. *J. Phys. Chem. Lett.* **2013**, *4*, 388–392.
- (8) Rosen, J.; Hutchings, G. S.; Lu, Q.; Rivera, S.; Zhou, Y.; Vlachos, D. G.; Jiao, F. Mechanistic Insights into the Electrochemical Reduction of CO₂ to CO on Nanostructured Ag Surfaces. *ACS Catal.* **2015**, *5*, 4293–4299.
- (9) Dunwell, M.; Luc, W.; Yan, Y.; Jiao, F.; Xu, B. Understanding Surface-Mediated Electrochemical Reactions: CO₂ Reduction and Beyond. *ACS Catal.* **2018**, *8*, 8121–8129.
- (10) Singh, M. R.; Goodpaster, J. D.; Weber, A. Z.; Head-Gordon, M.; Bell, A. T. Mechanistic Insights into Electrochemical Reduction of CO₂ over Ag Using Density Functional Theory and Transport Models. *Proc. Natl. Acad. Sci. U.S.A.* **2017**, *114*, E8812–E8821.
- (11) Chen, L. D.; Urushihara, M.; Chan, K.; Nørskov, J. K. Electric Field Effects in Electrochemical CO₂ Reduction. *ACS Catal.* **2016**, *6*, 7133–7139.
- (12) Dunwell, M.; Yang, X.; Setzler, B. P.; Anibal, J.; Yan, Y.; Xu, B. Examination of Near-Electrode Concentration Gradients and Kinetic Impacts on the Electrochemical Reduction of CO₂ Using Surface-Enhanced Infrared Spectroscopy. *ACS Catal.* **2018**, *8*, 3999–4008.
- (13) Goyal, A.; Marcandalli, G.; Mints, V. A.; Koper, M. T. M. Competition between CO₂ Reduction and Hydrogen Evolution on a Gold Electrode under Well-Defined Mass Transport Conditions. *J. Am. Chem. Soc.* **2020**, *142*, 4154–4161.
- (14) Varela, A. S.; Kroschel, M.; Reier, T.; Strasser, P. Controlling the Selectivity of CO₂ Electroreduction on Copper: The Effect of the Electrolyte Concentration and the Importance of the Local pH. *Catal. Today* **2016**, *260*, 8–13.
- (15) Clark, E. L.; Bell, A. T. Direct Observation of the Local Reaction Environment during the Electrochemical Reduction of CO₂. *J. Am. Chem. Soc.* **2018**, *140*, 7012–7020.
- (16) Kim, B.; Ma, S.; Molly Jhong, H.-R.; Kenis, P. J. A. Influence of Dilute Feed and pH on Electrochemical Reduction of CO₂ to CO on Ag in a Continuous Flow Electrolyzer. *Electrochim. Acta* **2015**, *166*, 271–276.
- (17) Hashiba, H.; Weng, L.-C.; Chen, Y.; Sato, H. K.; Yotsuhashi, S.; Xiang, C.; Weber, A. Z. Effects of Electrolyte Buffer Capacity on Surface Reactant Species and the Reaction Rate of CO₂ in Electrochemical CO₂ Reduction. *J. Phys. Chem. C* **2018**, *122*, 3719–3726.
- (18) Gupta, N.; Gattrell, M.; MacDougall, B. Calculation for the Cathode Surface Concentrations in the Electrochemical Reduction of CO₂ in KHCO₃ Solutions. *J. Appl. Electrochem.* **2006**, *36*, 161–172.
- (19) Singh, M. R.; Clark, E. L.; Bell, A. T. Effects of Electrolyte, Catalyst, and Membrane Composition and Operating Conditions on the Performance of Solar-Driven Electrochemical Reduction of Carbon Dioxide. *Phys. Chem. Chem. Phys.* **2015**, *17*, 18924–18936.
- (20) Raciti, D.; Mao, M.; Wang, C. Mass Transport Modelling for the Electroreduction of CO₂ on Cu Nanowires. *Nanotechnology* **2018**, *29*, No. 044001.
- (21) Ringe, S.; Morales-Guio, C. G.; Chen, L. D.; Fields, M.; Jaramillo, T. F.; Hahn, C.; Chan, K. Double Layer Charging Driven Carbon Dioxide Adsorption Limits the Rate of Electrochemical Carbon Dioxide Reduction on Gold. *Nat. Commun.* **2020**, *11*, No. 33.
- (22) Bohra, D.; Ledezma-Yanez, I.; Li, G.; de Jong, W.; Pidko, E. A.; Smith, W. A. Lateral Adsorbate Interactions Inhibit HCOO[−] While Promoting CO Selectivity for CO₂ Electrocatalysis on Silver. *Angew. Chem., Int. Ed.* **2019**, *58*, 1345–1349.
- (23) Clark, E. L.; Ringe, S.; Tang, M.; Walton, A.; Hahn, C.; Jaramillo, T. F.; Chan, K.; Bell, A. T. Influence of Atomic Surface Structure on the Activity of Ag for the Electrochemical Reduction of CO₂ to CO. *ACS Catal.* **2019**, *9*, 4006–4014.
- (24) Hoshi, N.; Kato, M.; Hori, Y. Electrochemical Reduction of CO₂ on Single Crystal Electrodes of Silver Ag(111), Ag(100) and Ag(110). *J. Electroanal. Chem.* **1997**, *440*, 283–286.
- (25) *Lange's Handbook of Chemistry*, 15th ed.; Dean, J. A.; Lange, N. A., Eds.; McGraw-Hill Handbooks; McGraw-Hill: New York, NY, 1999.
- (26) Hatsukade, T.; Kuhl, K. P.; Cave, E. R.; Abram, D. N.; Jaramillo, T. F. Insights into the Electrocatalytic Reduction of CO₂ on Metallic Silver Surfaces. *Phys. Chem. Chem. Phys.* **2014**, *16*, 13814–13819.
- (27) Dunwell, M.; Lu, Q.; Heyes, J. M.; Rosen, J.; Chen, J. G.; Yan, Y.; Jiao, F.; Xu, B. The Central Role of Bicarbonate in the Electrochemical Reduction of Carbon Dioxide on Gold. *J. Am. Chem. Soc.* **2017**, *139*, 3774–3783.
- (28) Back, S.; Yeom, M. S.; Jung, Y. Active Sites of Au and Ag Nanoparticle Catalysts for CO₂ Electroreduction to CO. *ACS Catal.* **2015**, *5*, 5089–5096.
- (29) Yoo, J. S.; Christensen, R.; Vegge, T.; Nørskov, J. K.; Studt, F. Theoretical Insight into the Trends That Guide the Electrochemical

Reduction of Carbon Dioxide to Formic Acid. *ChemSusChem* **2016**, *9*, 358–363.

(30) Liu, M.; Pang, Y.; Zhang, B.; De Luna, P.; Voznyy, O.; Xu, J.; Zheng, X.; Dinh, C. T.; Fan, F.; Cao, C.; de Arquer, F. P. G.; Safaei, T. S.; Mepham, A.; Klinskova, A.; Kumacheva, E.; Filleter, T.; Sinton, D.; Kelley, S. O.; Sargent, E. H. Enhanced Electrocatalytic CO₂ Reduction via Field-Induced Reagent Concentration. *Nature* **2016**, *537*, 382–386.

(31) Firet, N. J.; Smith, W. A. Probing the Reaction Mechanism of CO₂ Electroreduction over Ag Films via Operando Infrared Spectroscopy. *ACS Catal.* **2017**, *7*, 606–612.

(32) Liu, X.; Schlexer, P.; Xiao, J.; Ji, Y.; Wang, L.; Sandberg, R. B.; Tang, M.; Brown, K. S.; Peng, H.; Ringe, S.; Hahn, C.; Jaramillo, T. F.; Nørskov, J. K.; Chan, K. PH Effects on the Electrochemical Reduction of CO(2) towards C2 Products on Stepped Copper. *Nat. Commun.* **2019**, *10*, No. 32.

(33) Huang, J.; Zhang, J.; Eikerling, M. Unifying Theoretical Framework for Deciphering the Oxygen Reduction Reaction on Platinum. *Phys. Chem. Chem. Phys.* **2018**, *20*, 11776–11786.

(34) Wellendorff, J.; Lundgaard, K. T.; Møgelhøj, A.; Petzold, V.; Landis, D. D.; Nørskov, J. K.; Bligaard, T.; Jacobsen, K. W. Density Functionals for Surface Science: Exchange-Correlation Model Development with Bayesian Error Estimation. *Phys. Rev. B* **2012**, *85*, No. 235149.

(35) Huang, J. On Obtaining Double-Layer Capacitance and Potential of Zero Charge from Voltammetry. *J. Electroanal. Chem.* **2020**, *870*, No. 114243.

(36) Zhang, Z.; Gao, Y.; Chen, S.; Huang, J. Understanding Dynamics of Electrochemical Double Layers via a Modified Concentrated Solution Theory. *J. Electrochem. Soc.* **2020**, *167*, No. 013519.

(37) Chan, K.; Eikerling, M. A Pore-Scale Model of Oxygen Reduction in Ionomer-Free Catalyst Layers of PEFCs. *J. Electrochem. Soc.* **2011**, *158*, No. B18.

(38) Zhu, X.; Huang, J. Modeling Electrocatalytic Oxidation of Formic Acid at Platinum. *J. Electrochem. Soc.* **2020**, *167*, No. 013515.

(39) Huang, J.; Malek, A.; Zhang, J.; Eikerling, M. H. Non-Monotonic Surface Charging Behavior of Platinum: A Paradigm Change. *J. Phys. Chem. C* **2016**, *120*, 13587–13595.

(40) Malek, A.; Eikerling, M. H. Chemisorbed Oxygen at Pt(111): A DFT Study of Structural and Electronic Surface Properties. *Electrocatalysis* **2018**, *9*, 370–379.

(41) Singh, M. R.; Kwon, Y.; Lum, Y.; Ager, J. W.; Bell, A. T. Hydrolysis of Electrolyte Cations Enhances the Electrochemical Reduction of CO₂ over Ag and Cu. *J. Am. Chem. Soc.* **2016**, *138*, 13006–13012.

(42) Huang, J.; Zhu, X.; Eikerling, M. The Rate-Determining Term of Electrocatalytic Reactions with First-Order Kinetics. *Electrochim. Acta* **2021**, *393*, No. 139019.

(43) Weng, L.-C.; Bell, A. T.; Weber, A. Z. Modeling Gas-Diffusion Electrodes for CO₂ Reduction. *Phys. Chem. Chem. Phys.* **2018**, *20*, 16973–16984.

(44) Chen, Y.; Li, C. W.; Kanan, M. W. Aqueous CO₂ Reduction at Very Low Overpotential on Oxide-Derived Au Nanoparticles. *J. Am. Chem. Soc.* **2012**, *134*, 19969–19972.

(45) Wuttig, A.; Yoon, Y.; Ryu, J.; Surendranath, Y. Bicarbonate Is Not a General Acid in Au-Catalyzed CO₂ Electroreduction. *J. Am. Chem. Soc.* **2017**, *139*, 17109–17113.

(46) Bohra, D.; Chaudhry, J. H.; Burdyny, T.; Pidko, E. A.; Smith, W. A. Modeling the Electrical Double Layer to Understand the Reaction Environment in a CO₂ Electrocatalytic System. *Energy Environ. Sci.* **2019**, *12*, 3380–3389.

(47) Ringe, S.; Clark, E. L.; Resasco, J.; Walton, A.; Seger, B.; Bell, A. T.; Chan, K. Understanding Cation Effects in Electrochemical CO₂ Reduction. *Energy Environ. Sci.* **2019**, *12*, 3001–3014.

(48) Resasco, J.; Chen, L. D.; Clark, E.; Tsai, C.; Hahn, C.; Jaramillo, T. F.; Chan, K.; Bell, A. T. Promoter Effects of Alkali Metal Cations on the Electrochemical Reduction of Carbon Dioxide. *J. Am. Chem. Soc.* **2017**, *139*, 11277–11287.

(49) Huang, J.; Li, M.; Eslamibidgoli, M. J.; Eikerling, M.; Groß, A. Cation Overcrowding Effect on the Oxygen Evolution Reaction. *JACS Au* **2021**, *1*, 1752–1765.

(50) Wuttig, A.; Yaguchi, M.; Motobayashi, K.; Osawa, M.; Surendranath, Y. Inhibited Proton Transfer Enhances Au-Catalyzed CO₂-to-Fuels Selectivity. *Proc. Natl. Acad. Sci. U.S.A.* **2016**, *113*, E4585–E4593.